A Finite Volume Framework for the Fully Implicit Thermal-Hydro-Mechanical-Compositional Modeling in Geo-Energy Applications

Novikov, A.; Saifullin, I.; Hajibeygi, H.; Voskov, D.

DOI
10.3997/2214-4609.202437088

Publication date
2024

Document Version
Final published version

Published in
European Conference on the Mathematics of Geological Reservoirs, ECMOR 2024

Citation (APA)
Novikov, A., Saifullin, I., Hajibeygi, H., & Voskov, D. (2024). A Finite Volume Framework for the Fully Implicit Thermal-Hydro-Mechanical-Compositional Modeling in Geo-Energy Applications. In *European Conference on the Mathematics of Geological Reservoirs, ECMOR 2024* (Vol. 2, pp. 971-990). EAGE. https://doi.org/10.3997/2214-4609.202437088

ECMOR 2024
European Conference on the Mathematics of Geological Reservoirs
EAGE

A Finite Volume Framework for the Fully Implicit Thermal-Hydro-Mechanical-Compositional Modeling in Geo-Energy Applications

A. Novikov[1], I. Saifullin[1], H. Hajibeygi[1], D. Voskov[1,2]
[1] Delft University of Technology; [2] Stanford University

Summary

The role of Thermal-Hydro-Mechanical-Compositional analysis in the development of geo-energy resources has been amplified in recent years. As an example, challenges such as wellbore stability, land subsidence and induced seismicity highlight the necessity for comprehensive geomechanical evaluations which are then coupled with thermo-hydrodynamical processes within the reservoir. Numerical simulations of the coupled thermo-poromechanical processes provide a general-purpose tool capable of performing these evaluations at both continuum laboratory and field scales. However, efficient integration of the coupled system of fluid mass, energy and momentum conservation equations poses multiple numerical and implementation difficulties, such as combining different numerical methods on staggered grids and associated limitations on admissible grids.

This paper introduces a new fully-implicit scheme of the Finite Volume Method (FVM) for modeling thermal compositional flow in thermo-poroelastic rocks. The scheme uses the gradient-based variant of coupled multi-point approximations of fluid mass, momentum, heat convection and conduction fluxes, which are derived from their respective local balances. The novelty of the scheme is that it incorporates temperature into the approximation of these fluxes. Consequently, the approximation of displacement gradients depends on temperatures, while the approximation of temperature itself is derived from the balance of heat conduction fluxes. At the same time, we utilize a single-point upstream weighting for the temperature-dependent terms in heat convection fluxes. The resulting scheme respects the local balance of fluxes in the presence of temperature gradients. Besides, it also supports star-shaped and various boundary conditions. Overall, the scheme represents a unified FVM-based approach for the integration of all conservation laws relevant to geo-energy applications on a cell-centered collocated grid. Furthermore, the implemented two-stage block-partitioned preconditioning strategy enables the efficient solution of obtained linear systems. The proposed modeling framework has been implemented in an open-source Delft Advanced Research Terra Simulator (DARTS). Moreover, the flexibility regarding compositional fluid properties is reinforced by the Operator-Based Linearization (OBL) technique incorporated into DARTS.

The proposed modeling framework has undergone rigorous validation in convergence study, and comparisons against established analytical and numerical solutions. The framework covers advanced physical phenomena including thermal expansion and contraction, porosity dependent on pressure, temperature and strain, and multiphase flow with phase changes and chemical alterations. The framework capabilities and the performance of the preconditioning strategy have been assessed in the mechanical extension of the 10th SPE Comparative study (SPE10) model.

Introduction

Geomechanics is crucial for the safe and optimal operation of modern geo-energy applications (Zoback, 2007). Changes in subsurface conditions (e.g., pressure depletion in gas production) often cause subsidence, can initiate induced seismicity, and cause serious damages to surface infrastructures (Buijze et al., 2020; Pluymakers et al., 2023). In geothermal operations, the re-injection of cooler fluid causes stress and strain changes that can potentially (re-)activate faults and lead to induced seismic activity (Ellsworth et al., 2019; Schultz et al., 2022). The development of CO_2 geological storage involves a complex interaction of thermal, hydraulic, mechanical, and chemical processes which collectively change the in-situ stress state, affect fault stability, and can lead to fault activation, CO_2 leakage and seismicity (Rohmer et al., 2016; Cheng et al., 2023). Therefore, the successful and risk-free exploitation of subsurface resources depends on the development of robust and efficient computational techniques for modeling the coupled geomechanics and hydrothermal processes.

The Finite Volume Method (FVM) has recently been seen as a promissing technique for modeling of geomechanics, especially when mechanical interactions are modeled in a fully coupled manner with the flow and transport of mass and energy. The FVM is attractive because it represents an integral form of conservation laws. Recent literature highlights its development for geomechanical simulations with both staggered (Deb and Jenny, 2017a; Sokolova et al., 2019; Shokrollahzadeh Behbahani et al., 2022) and collocated grids (Nordbotten, 2014; Terekhov and Tchelepi, 2020; Novikov et al., 2022). The advantages of FVM include the local preservation of momentum balance, discontinuous basis functions, and seamless integration with fluid mass and energy balance solvers.

Coupling different physics within thermal-hydraulic-mechanical-compositional (THMC) simulations is challenging. Some authors (Deb and Jenny, 2017b; Garipov et al., 2018) use fixed-stress splitting algorithms (Settari and Mourits, 1998; Kim et al., 2011) to decouple mechanics and flow equations. These are a form of sequential implicit (SI) solution scheme and often lead to more efficient simulations than a fully implicit (FI) approach. However, sequential schemes introduce certain restrictions on time step sizes. On the other hand, FI schemes (Sokolova et al., 2019; Garipov et al., 2016, 2018) provide unconditionally convergent solutions and are often more robust and convenient approaches for the investigation of complex multiphysics problems. When comparing FI and SI approaches designed using the most efficient numerical techniques (e.g., proper linear preconditioning), the FI approach often outperforms the SI approach in the context of coupled thermo-compositional-mechanics simulation (Garipov et al., 2018).

Although the FI approach does not impose any restriction on time step size, it requires efficient nonlinear and linear solution strategies for high-resolution models. One such strategy is to construct a preconditioner based on the idea of the SI approach. In White et al. (2016), the authors employ a fixed-stress splitting concept in a sparse approximation of the Schur complement to obtain a block-preconditioned solution strategy. Later this approach was combined with a constrained pressure residual (CPR) preconditioner to construct a robust and effective solution strategy for coupled multiphase flow and mechanics (Klevtsov et al., 2016; White et al., 2019).

In this study, we present a novel cell-centered collocated FI multi-point FVM scheme for THMC simulation of subsurface reservoirs. It treats mass, energy, and momentum fluxes in a unified vector form within the framework of FVM, resulting in a simplified formulation. The framework can be used to resolve the coupled THMC processes in arbitrarily anisotropic thermoporoelastic rocks on unstructured polyhedral grids with a minimum number of degrees of freedom per cell. It is also capable of handling material heterogeneities while preserving mass, energy and momentum balances. The framework supports multiphase compositional fluid physics, including phase equilibrium and chemical reactions resolved through operator-based linearization (Khait and Voskov, 2017). To further enhance the scalability of the framework, a block-partitioned preconditioning strategy is implemented. The developed computational capabilities are verified in benchmarks.

These methods are implemented in the open-source Delft Advanced Research Terra Simulator (open-

DARTS) (Voskov et al., 2023). open-DARTS is a scalable parallel simulator, which has been successfully applied to the modeling of hydrocarbon (Khait and Voskov, 2018a; Lyu et al., 2021a), geothermal (Khait and Voskov, 2018b; Wang et al., 2020), CO_2 sequestration (Kala and Voskov, 2020; Lyu et al., 2021b) applications, as well as evaluating potential to fault reactivation and seismicity (Novikov et al., 2022; Novikov, 2024). This study further extends the coupling between geomechanical modeling and the advanced hydro-thermal modeling capabilities of open-DARTS, making it a fully coupled THMC simulator for complex geo-energy applications.

Governing Equations

Continuous formulation

The system of various conservation laws governs the thermohydromechanical response of porous rock saturated by compositional fluid flow. It includes the mass balances of fluid components $i = 1,\dots,\mathrm{n}_c$, the energy balance and the momentum balance (Coussy, 2003) that can be written as

$$\frac{\partial}{\partial t}\left(\phi\sum_{\alpha}^{\mathrm{n}_p}\mathrm{x}_{i\alpha}\mathrm{s}_\alpha\rho_\alpha\right)+\nabla\cdot\left(\sum_{\alpha}^{\mathrm{n}_p}\mathrm{x}_{i\alpha}\rho_\alpha\mathbf{q}_\alpha^{(\mathrm{f})}\right)-\sum_{\alpha}^{\mathrm{n}_p}\mathrm{x}_{i\alpha}\rho_\alpha\mathrm{r}_\alpha=0,\quad i=1,\dots,\mathrm{n}_c, \tag{1}$$

$$\frac{\partial}{\partial t}\left((1-\phi)\rho_s\mathrm{U}_s+\phi\sum_{\alpha}^{\mathrm{n}_p}\mathrm{s}_\alpha\rho_\alpha\mathrm{U}_\alpha\right)+\nabla\cdot\left(\sum_{\alpha}^{\mathrm{n}_p}\left(\rho_\alpha\mathrm{h}_\alpha\mathbf{q}_\alpha^{(\mathrm{f})}+\phi\mathrm{s}_\alpha\mathbf{q}_\alpha^{(\theta)}\right)+(1-\phi)\mathbf{q}_s^{(\theta)}\right)-\sum_{\alpha}^{\mathrm{n}_p}\rho_\alpha\mathrm{h}_\alpha\mathrm{r}_\alpha=0, \tag{2}$$

$$-\nabla\cdot\boldsymbol{\sigma}-\left((1-\phi)\rho_s+\phi\sum_{\alpha}^{\mathrm{n}_p}\mathrm{s}_\alpha\rho_\alpha\right)\mathrm{g}\nabla\mathrm{z}=0, \tag{3}$$

where subscripts s,α denote rock matrix and fluid phases $1,\dots,\mathrm{n}_p$ respectively, ϕ is porosity, $\mathrm{x}_{i\alpha}$ are compositions, s_α are phase saturations, ρ_α are phase densities, $\mathbf{q}_\alpha^{(\mathrm{f})}$ are Darcy's phase velocities, r_α are phase source terms, $\mathrm{U}_s,\mathrm{U}_\alpha$ are the internal energies of rock matrix and fluid phases respectively, h_α are phase enthalpies, $\mathbf{q}_s^{(\theta)}$ and $\mathbf{q}_\alpha^{(\theta)}$ are the vectors of heat conduction fluxes in rock matrix s and in fluid phase α correspondingly, $\boldsymbol{\sigma}$ is the rank-two total Couchy's stress tensor, ρ_s is the density of rock matrix, g is the gravitational acceleration, z is depth.

The balance laws in Eqs. (1)-(3) are subjected to the following constitutive relationships (Coussy, 2003; Zhao and Borja, 2020)

$$\mathbf{q}_\alpha^{(\mathrm{f})}=-\frac{k_{r\alpha}\mathbf{K}}{\mu_\alpha}\left(\nabla\mathrm{p}-\rho_\alpha\mathrm{g}\nabla\mathrm{z}\right), \tag{4}$$

$$\mathbf{q}_\alpha^{(\theta)}=-\boldsymbol{\Lambda}_\alpha\nabla\mathrm{T}, \tag{5}$$

$$\phi-\phi_0=\frac{(\psi-\phi_0)(1-\psi)}{\mathrm{K}_s}(\mathrm{p}-\mathrm{p}_0)+\mathbf{B}:\nabla^s(\mathbf{u}-\mathbf{u}_0)+\alpha_\phi(\mathrm{T}-\mathrm{T}_0), \tag{6}$$

$$\boldsymbol{\sigma}-\boldsymbol{\sigma}_0=\mathbb{C}:\nabla^s(\mathbf{u}-\mathbf{u}_0)-(\mathrm{p}-\mathrm{p}_0)\mathbf{B}-(\mathrm{T}-\mathrm{T}_0)\mathbf{A}, \tag{7}$$

$$\rho_\alpha=\rho_\alpha(\mathrm{p},\mathrm{T},\mathrm{x}_{i\alpha}),\quad \mu_\alpha=\mu_\alpha(\mathrm{p},\mathrm{T},\mathrm{x}_{i\alpha}),\quad \mathrm{h}_\alpha=\mathrm{c}_\alpha(\mathrm{T}-\mathrm{T}_0),\quad \mathrm{U}_\alpha=\mathrm{h}_\alpha-\frac{\mathrm{p}}{\rho_\alpha}, \tag{8}$$

$$\mathrm{U}_s=\mathrm{c}_s(\mathrm{T}-\mathrm{T}_0), \tag{9}$$

$$\varphi_{i\alpha}(\mathrm{p},\mathrm{T},\mathrm{x}_{i\alpha})-\varphi_{i\beta}(\mathrm{p},\mathrm{T},\mathrm{x}_{i\beta})=0,\quad \forall\alpha\neq\beta=1,\dots,\mathrm{n}_p,\ i=1,\dots,\mathrm{n}_c,$$

$$\sum_{\alpha}^{\mathrm{n}_p}\mathrm{s}_\alpha=1,\quad \sum_{i}^{\mathrm{n}_c}\mathrm{x}_{i\alpha}=1,\quad \alpha=1,\dots,\mathrm{n}_p, \tag{10}$$

where $k_{r\alpha}$ are relative phase permeabilities, $\mathbf{K}$ is the rank-two permeability tensor, p is pore pressure, μ_α are phase viscosities, $\boldsymbol{\Lambda}_s$ and $\boldsymbol{\Lambda}_\alpha$ are the rank-two heat conduction tensors of rock matrix and fluid phases respectively, $\nabla^s\mathbf{u}=(\nabla\mathbf{u}+(\nabla\mathbf{u})^T)/2$ is the matrix of symmetric gradients of displacements, $\mathbf{B}$ is the rank-two tensor of Biot's coefficients (Coussy, 2003; Zhao and Borja, 2020; Cheng, 1997), $\psi=I_1(\mathbf{B})/3$ is one-third of the first invariant of $\mathbf{B}$, K_s is rock matrix drained bulk modulus, α_ϕ is the volumetric coefficient of rock matrix thermal dilation, $\mathbb{C}$ is the rank-four drained stiffness tensor, $\mathbf{A}$ is the rank-two rock matrix thermal dilation tensor, $\mathbf{u}$ is a vector of displacements, c_s and c_α are constant-pressure heat capacities of rock matrix and fluid phases correspondingly, $\varphi_{i\alpha}$ is the fugacity of component i in phase

α, and the subscript 0 denotes the reference state of a variable, i.e.,

$$\boldsymbol{\sigma}_0 = \boldsymbol{\sigma}(\mathbf{u}_0, \mathrm{p}_0, \mathrm{T}_0), \quad \phi_0 = \phi(\mathbf{u}_0, \mathrm{p}_0, \mathrm{T}_0). \tag{11}$$

Eqs. (4) and (5) represent Darcy's and Fourier's laws that define fluid and heat conduction fluxes caused by spatial variation of pore pressure and temperature respectively, Eqs. (6) and (7) represent porosity and stress changes in anisotropic thermoporoelastic media under the assumption of infinitesimal strains, the fluid properties, i.e density, viscosity, enthalpy and internal energy are defined in Eq. (8) while rock matrix internal energy is specified in Eq. (9), the distribution of components between fluid phases is evaluated from thermodynamic equilibrium written in Eq. (10). We do not consider the effect of capillary forces between fluid phases neither in the Darcy's law in Eq. (4) nor in the phase equilibrium in Eq. (10). All variables have been listed in the Nomenclature section at the end of the paper.

The projection of stress tensor $\boldsymbol{\sigma}$ to an interface with unit normal vector $\mathbf{n}$ is called total traction vector $\mathbf{f}$ and defined as

$$\mathbf{f} = -\boldsymbol{\sigma}\mathbf{n}, \tag{12}$$

where the negative sign is motivated by the sign of the corresponding term in the momentum balance in Eq. (3). Traction vector can be decomposed into normal f_N and tangential components $\mathbf{f}_T$ as

$$\mathbf{f} = \mathrm{f}_N\mathbf{n} + \mathbf{f}_T, \quad \mathrm{f}_N = -\mathbf{n}^T\boldsymbol{\sigma}\mathbf{n}, \quad \mathbf{f}_T = (\mathbf{I} - \mathbf{n}\mathbf{n}^T)\mathbf{f}, \tag{13}$$

where $-\mathrm{f}_N$ and $|\mathbf{f}_T|$ are called normal and shear stresses, respectively and $\mathbf{I}$ is an identity matrix.

For the system of balance laws in Eqs. (1)-(3) and constitutive relationships in Eqs. (4)-(10) we consider boundary conditions in the following form

$$\alpha_p \mathrm{p}_b + \beta_p \left(\mathbf{K}\mathbf{n} \cdot (\nabla \mathrm{p} - \rho_\mathrm{f} \mathrm{g} \nabla \mathrm{z})\right)_b = \gamma_p, \tag{14}$$
$$\alpha_\theta \mathrm{T}_b + \beta_\theta (\boldsymbol{\Lambda}\mathbf{n} \cdot \nabla \mathrm{T})_b = \gamma_\theta, \tag{15}$$
$$\mathbf{n}^T \left(\alpha_n \mathbf{u}_b + \beta_n \mathbf{f}_b\right) = \gamma_n, \tag{16}$$
$$(\mathbf{I} - \mathbf{n}\mathbf{n}^T)\left(\alpha_t \mathbf{u}_b + \beta_t \mathbf{f}_b\right) = \boldsymbol{\gamma}_t, \tag{17}$$

where subscript b denotes the property evaluated at the boundary, α_p, β_p, $\alpha_\theta, \beta_\theta$, α_n, β_n and α_t, β_t are coefficients that determine the particular kind of boundary conditions, while $\gamma_p, \gamma_\theta, \gamma_n$ and $\boldsymbol{\gamma}_t$ represent the values the corresponding conditions are assigned to, ρ_f stands for the effective density of fluid flux estimated as

$$\rho_\mathrm{f} = \sum_{\alpha}^{\mathrm{n}_p} \mathrm{s}_\alpha \rho_\alpha. \tag{18}$$

Additionally, Eq. (14) defines the boundary condition for fluid mass balance, Eq. (15) specifies the boundary condition for energy balance, Eqs. (16), (17) represent normal and tangential boundary conditions for the momentum balance respectively

Eqs. (14)-(17) describe a broad range of possible boundary conditions, including

- Dirichlet for mechanics ($\alpha_n = \alpha_t = 1$, $\beta_n = \beta_t = 0$),
- distributed force loading ($\alpha_n = \alpha_t = 0$, $\beta_n = \beta_t = 1$),
- free boundary ($\alpha_n = \alpha_t = \gamma_n = 0$, $\beta_n = \beta_t = 1$, $\boldsymbol{\gamma}_t = \mathbf{0}$), and
- roller conditions ($\alpha_n = \beta_t = 1$, $\beta_n = \gamma_n = \alpha_t = 0$, $\boldsymbol{\gamma}_t = \mathbf{0}$) for mechanics; and
- Dirichlet ($\alpha_p = \alpha_\theta = 1$, $\beta_p = \beta_\theta = 0$) and
- Neumann ($\alpha_p = \alpha_\theta = 0$, $\beta_p = \beta_\theta = 1$) conditions for flow and energy.

Eqs. (1)-(3) with substituted Eqs. (4)-(10) represent a system of $n_c + 4$ equations with respect to unknown pressure p, compositions $x_{i\alpha}$, temperature T and displacements $\mathbf{u}$. The problem definition is further refined by incorporating boundary conditions as specified in Eqs. (14)-(17), along with the initial values assigned to the unknown variables.

Discrete formulation

Finite Volume scheme for the system of partial differential equations (1)-(3) can be written in the following residual form

$$\mathbf{H}_j^{n+1} = \begin{bmatrix} \mathbf{H}_m \\ H_e \\ \mathbf{H}_{mom} \end{bmatrix}_j^{n+1} = V_j \begin{bmatrix} \mathfrak{a}_i^{n+1} - \mathfrak{a}_i^n - \Delta t_n \mathfrak{r}_i^{n+1} \\ \mathfrak{a}_e^{n+1} - \mathfrak{a}_e^n - \Delta t_n \mathfrak{r}_e^{n+1} \\ \mathfrak{r}_{mom}^{n+1} \end{bmatrix} + \sum_{\beta \in \partial V_j} \delta_\beta \begin{bmatrix} \Delta t_n \mathfrak{f}_{i,\beta}^{n+1} \\ \Delta t_n \mathfrak{f}_{e,\beta}^{n+1} \\ \mathbf{f}_\beta^{n+1} \end{bmatrix} = \mathbf{0}, \tag{19}$$

where

$$\mathfrak{a}_i^{n+1} = \left(\phi \sum_\alpha^{n_p} x_{i\alpha} s_\alpha \rho_\alpha \right)_j^{n+1}, \qquad \mathfrak{r}_i^{n+1} = \left(\sum_\alpha^{n_p} x_{i\alpha} \rho_\alpha r_\alpha \right)_j^{n+1},$$

$$\mathfrak{a}_e^{n+1} = \left((1-\phi)\rho_s U_s + \phi \sum_\alpha^{n_p} \rho_\alpha U_\alpha \right)_j^{n+1}, \qquad \mathfrak{r}_e^{n+1} = \left(\sum_\alpha^{n_p} \rho_\alpha h_\alpha r_\alpha \right)_j^{n+1},$$

$$\mathfrak{r}_{mom}^{n+1} = -\left((1-\phi)\rho_s + \phi \sum_\alpha^{n_p} s_\alpha \rho_\alpha \right)_j^{n+1} g \nabla z,$$

$$\mathfrak{f}_{i,\beta}^{n+1} = \sum_\alpha^{n_p} \left(x_{i\alpha} \rho_\alpha k_{r\alpha} \mu_\alpha^{-1} q_{\alpha,\beta}^{(f),n+1} \right),$$

$$\mathfrak{f}_{e,\beta}^{n+1} = \sum_\alpha^{n_p} \left((h_\alpha \rho_\alpha)_u^{n+1} q_{\alpha,\beta}^{(f),n+1} - \phi_j^{n+1} s_{\alpha,u}^{n+1} q_{\alpha,\beta}^{(\theta),n+1} - (1-\phi_j^{n+1}) q_{s,\beta}^{(\theta),n+1} \right).$$

Additionally, $\mathbf{H}_m, H_e$ and $\mathbf{H}_{mom}$ denote the residuals of the mass balances of fluid components, energy balance and momentum balance respectively, written for cell j; terms $\mathfrak{a}, \mathfrak{r}$ and $\mathfrak{f}$ stand for accumulation, source and flux terms, respectively. Furthermore, V_j is the volume of a cell j, Δt_n is n-th timestep, subscript j denotes the properties evaluated at the center of corresponding cell, subscript β denotes the properties approximated at the center of corresponding interface, subscript u denotes the upwind approximation, supercripts n and $n+1$ denote the current and the next time layers respectively, δ_β is the surface of interface β. Besides, we use the following notations

$$q_{\alpha,\beta}^{(f)} = -\left(\mathbf{K}\mathbf{n} \cdot (\nabla p - \rho_\alpha g \nabla z) \right)_\beta, \quad q_\beta^{(\theta)} = -\left(\mathbf{\Lambda}\mathbf{n} \cdot \nabla T \right)_\beta, \tag{20}$$

where $q_\alpha^{(f)}$ is the Darcy's flux from Eq. (4), $q_\alpha^{(\theta)}$ is the Fourier's heat conduction flux from Eq. (5).

Moreover, we approximate porosity defined in Eq. (6) as

$$\phi_j^{n+1} = \left[\phi_0 + \frac{(\psi - \phi_0)(1-\psi)}{K_s} (p - p_0) + \alpha_\phi (T - T_0) \right]_j^{n+1} + \frac{1}{V_j} \sum_{\beta \in \partial V_j} \delta_\beta \left(\tilde{q}_\beta^{n+1} - \tilde{q}_\beta^n \right). \tag{21}$$

where the flux $\tilde{q}_\beta$ is defined as

$$\tilde{q}_\beta = \left(\mathbf{u}_\beta - \mathbf{u}_j \right) \cdot (\mathbf{B}\mathbf{n})_j. \tag{22}$$

Discretization

Approximation of fluxes

Many numerical schemes of FVM rely on flux approximation. Widely exploited in reservoir engineering, the Two-Point Flux Approximation (TPFA) is applicable for diffusive fluxes under certain constraints. The Multi-Point Flux Approximation (MPFA) (Aavatsmark et al., 1996; Edwards and Rogers, 1998) is not limited by those constraints but can introduce instability (Keilegavlen and Aavatsmark, 2008). Its extension to momentum fluxes in elasticity systems is called Multi-Point Stress Approximation (Nordbotten, 2014), which has been combined into the MPFA-MPSA approach for the coupled modeling of poroelasticity (Nordbotten, 2016) and thermoporoelasticity (Stefansson et al., 2020, 2021) systems. To improve the stability properties of multi-point schemes, a family of weighted schemes has been developed (Schneider et al., 2018) resulting in the evolution of nonlinear FVM schemes (Le Potier, 2005; Terekhov et al., 2017; Tripuraneni et al., 2023).

In this work, we extend the gradient-based weighted scheme initially proposed for poroelasticity systems (Terekhov, 2020), to thermoporoelasticity systems. For this purpose, we utilize MPFA approximation for the approximation of heat conduction and the interpolation of temperature at the interface. At the same time, we employ a single-point upstream (SPU) weighting for the temperature-dependent terms in heat convection fluxes.

The approximation of fluxes can be derived from the continuity of unknowns $\mathbf{d} = \left[\mathrm{p}, \mathrm{T}, \mathbf{u}^T\right]$ and associated fluxes. Below we impose the continuity of Darcy's, heat conduction and momentum fluxes which, along with the continuity of unknowns, constitute the local problem. It can be written for the interior interface with unit normal vector $\mathbf{n}$ and belonging to cells 1 and 2 as

$$\begin{aligned}
\mathbf{d}_{\beta 1} = \mathbf{d}_1 + \left[\mathbf{I} \otimes (\mathbf{x}_\beta - \mathbf{x}_1)^T\right](\nabla \otimes \mathbf{d}_1) &= \mathbf{d}_2 + \left[\mathbf{I} \otimes (\mathbf{x}_\beta - \mathbf{x}_2)^T\right](\nabla \otimes \mathbf{d}_2) = \mathbf{d}_{\beta 2}, && (23)\\
-(\nabla \mathrm{p}_1 - \rho_\mathrm{f} \mathrm{g} \nabla \mathrm{z}) \cdot \mathbf{K}_1 \mathbf{n} &= -(\nabla \mathrm{p}_2 - \rho_\mathrm{f} \mathrm{g} \nabla \mathrm{z}) \cdot \mathbf{K}_2 \mathbf{n}, && (24)\\
-\nabla \mathrm{T}_1 \cdot \mathbf{\Lambda}_1 \mathbf{n} &= -\nabla \mathrm{T}_2 \cdot \mathbf{\Lambda}_2 \mathbf{n}, && (25)\\
-\left[\mathbf{I} \otimes \mathbf{n}^T\right] \mathbf{S}_1 (\nabla \otimes \mathbf{u}_1) + \mathrm{p}_{\beta 1} \mathbf{B}_1 \mathbf{n} + \mathrm{T}_{\beta 1} \mathbf{A}_1 \mathbf{n} &= -\left[\mathbf{I} \otimes \mathbf{n}^T\right] \mathbf{S}_2 (\nabla \otimes \mathbf{u}_2) + \mathrm{p}_{\beta 2} \mathbf{B}_2 \mathbf{n} + \mathrm{T}_{\beta 2} \mathbf{A}_2 \mathbf{n}, && (26)
\end{aligned}$$

where $\mathbf{d}_1$ and $\mathbf{d}_2$ are unknowns at the cell centers, $\mathbf{x}_1$ and $\mathbf{x}_2$ are the positions of the cell centers, $\otimes$ denotes the Kronecker product, $\mathbf{x}_\beta$ denotes the center of the interface, $\mathbf{I} \otimes (\mathbf{x}_\beta - \mathbf{x}_1)^T$ and $\mathbf{I} \otimes (\mathbf{x}_\beta - \mathbf{x}_2)^T$ represent 5×15 matrices constructed as

$$\mathbf{I} \otimes (\mathbf{x}_\beta - \mathbf{x}_i)^T = \begin{pmatrix} (\mathbf{x}_\beta - \mathbf{x}_i)^T & & & & \\ & (\mathbf{x}_\beta - \mathbf{x}_i)^T & & & \\ & & (\mathbf{x}_\beta - \mathbf{x}_i)^T & & \\ & & & (\mathbf{x}_\beta - \mathbf{x}_i)^T & \\ & & & & (\mathbf{x}_\beta - \mathbf{x}_i)^T \end{pmatrix}, \quad i = 1,2,$$

$\mathbf{I} \otimes \mathbf{n}^T$ stands for 3×9 matrix constructed in a similar way, $\nabla \otimes \mathbf{d}_1$, $\nabla \otimes \mathbf{d}_2$ and $\nabla \otimes \mathbf{u}_1$, $\nabla \otimes \mathbf{u}_2$ are 15×1 and 9×1 vectors respectively, constructed as

$$\nabla \otimes \mathbf{d}_i = \begin{pmatrix} \nabla \mathrm{p} \\ \nabla \mathrm{T} \\ \nabla \otimes \mathbf{u} \end{pmatrix}_i = \begin{pmatrix} \nabla \mathrm{p} \\ \nabla \mathrm{T} \\ \nabla \mathrm{u}_x \\ \nabla \mathrm{u}_y \\ \nabla \mathrm{u}_z \end{pmatrix}_i, \quad i = 1,2, \qquad (27)$$

where $[\mathrm{u}_x \mathrm{u}_y \mathrm{u}_z]^T$ are the components of displacement vector $\mathbf{u}$, $\mathbf{S}_1 = \mathbf{\Gamma} \mathbf{C}_1 \mathbf{\Gamma}^T$, $\mathbf{S}_2 = \mathbf{\Gamma} \mathbf{C}_2 \mathbf{\Gamma}^T$ are 9×9 matrices where $\mathbf{C}$ denotes a 6×6 symmetric stiffness matrix in Voigt notation and

$$\mathbf{\Gamma}^T = \begin{bmatrix} 1&0&0&0&0&0&0&0&0 \\ 0&0&0&0&1&0&0&0&0 \\ 0&0&0&0&0&0&0&0&1 \\ 0&0&0&0&0&1&0&1&0 \\ 0&0&1&0&0&0&1&0&0 \\ 0&1&0&1&0&0&0&0&0 \end{bmatrix}.$$

Flux balances in Eqs. (24), (25) and (26) stem from Darcy's, Fourier's and momentum fluxes in Eqs. (19). While the last one takes into account all contributions to total momentum flux, the local balance of flux mass in Eq. (24) neglects the fluxes caused by matrix movement and molecular diffusion. Additionally, the local balance of energy in Eq. (25) neglects heat convection fluxes. However, the conservation of Darcy's fluxes in Eq. (24) and the use of SPU approximation for advection (mobility) multipliers can guarantee the sufficiency of Eq. (25) for the conservation of cumulative heat convection and conduction flux.

It is clearly seen from Eqs. (23)-(26) that the local problem can be split into three subproblems: fluid mass, heat and momentum. The fluid mass and heat subproblems are completely independent while the momentum subproblem depends on them. Therefore, we first consider the necessary approximations derived from the fluid mass and heat subproblems.

For the derivation of MPFA approximation of Darcy's and Fourier's fluxes, pressure and temperature interpolations we employ the co-normal decomposition and gradient-based approach (Terekhov et al., 2017). The co-normal decomposition implies the split of vectors $\mathbf{Kn}$, $\mathbf{\Lambda n}$ and gradients $\nabla \mathrm{p}, \nabla \mathrm{T}$ into normal and tangential projections with respect to an interface. The gradient-based approach evaluates the approximations in a two-stage procedure. In the first stage, it reconstructs the gradients of unknowns $\nabla \mathrm{p}, \nabla \mathrm{T}$ from local problems in Eqs. (23), (24) and Eqs. (23), (25), respectively. In the second stage, it substitutes the approximations of gradients obtained in the first stage into the necessary MPFA approximations or interpolations of unknowns.

The same approach is utilized for the multi-point approximation of momentum fluxes, i.e. tractions, and for the interpolation of displacements. We use the co-normal decomposition of $\left[\mathbf{I} \otimes \mathbf{n}^T\right] \mathbf{S}$ and gradients $\nabla \otimes \mathbf{u}$. In the first stage, we reconstruct gradients while in the second stage, we assemble all necessary approximations.

The approximations of fluxes at boundary interfaces must satisfy corresponding boundary conditions defined in Eqs. (14)-(17). They replace the local problem, which we use for interior interfaces, and allow meaningful flux approximations to be derived at the domain's boundaries. We employ the single-side approximations from the left-hand side of Eqs. (23)-(26). Their substitution to the boundary conditions allows us to derive corresponding equations for gradient reconstruction, multi-point approximation and interpolation.

Reconstruction of gradients

The reconstruction of pressure and temperature gradients can be performed independently. Bringing together the equations with respect to pressure and temperature gradients for N considered interfaces of the j-th cell, we build up the independent systems

$$\mathbf{M}_j^p \nabla \mathrm{p}_j = \mathbf{D}_j^p \boldsymbol{\psi}_j^p, \quad \mathbf{M}_j^\theta \nabla \mathrm{T}_j = \mathbf{D}_j^\theta \boldsymbol{\psi}_j^\theta, \tag{28}$$

where $\mathbf{M}_j^p$ and $\mathbf{M}_j^\theta$ are $N \times 3$ matrices and $\mathbf{D}_j^p$ and $\mathbf{D}_j^\theta$ are $N \times (N+1)$ matrices of coefficients in front of the corresponding unknowns at the right-hand side, while $\boldsymbol{\psi}_j^p$ and $\boldsymbol{\psi}_j^\theta$ are $(N+1) \times 1$ vectors of $N+1$ unknowns or free terms in the right-hand side of boundary equations.

The solution of Eqs. (28) can be obtained in a least-squares sense as

$$\nabla \mathrm{p}_j = (\mathbf{M}_j^{pT} \mathbf{M}_j^p)^{-1} \mathbf{M}_j^{pT} \mathbf{D}_j^p \boldsymbol{\psi}_i^p, \quad \nabla \mathrm{T}_j = (\mathbf{M}_j^{\theta T} \mathbf{M}_j^\theta)^{-1} \mathbf{M}_j^{\theta T} \mathbf{D}_j^\theta \boldsymbol{\psi}_i^\theta. \tag{29}$$

The reconstruction of displacement gradients depends on pressure and temperature gradients. Thus, we evaluate pressure and temperature gradients in all cells first and, subsequently, substitute them into the reconstruction of displacement gradients. We employ the same approach for the reconstruction of displacement gradients, i.e. assemble N equations into the system

$$\mathbf{M}_j^u (\nabla \otimes \mathbf{u}_j) = \mathbf{D}_j^u \boldsymbol{\psi}_j^u, \tag{30}$$

for every j-th cell, where $\mathbf{M}_j^u$ is a $3N \times 9$ matrix, and $\mathbf{D}_j^u$ is $3N \times 5(N+1)$ matrix of coefficients in front of the corresponding unknowns at the right-hand side, while $\boldsymbol{\psi}_j^u$ is $5(N+1) \times 1$ vectors of $5(N+1)$ unknowns or free terms in the right-hand side of boundary equations. The least-squares solution of the system in Eq. (30) is

$$\nabla \otimes \mathbf{u}_j = (\mathbf{M}_j^{uT} \mathbf{M}_j^u)^{-1} \mathbf{M}_j^{uT} \mathbf{D}_j^u \boldsymbol{\psi}_i^u. \tag{31}$$

The flux approximations and interpolations depend on the tangential projections $\boldsymbol{\xi}_\tau$ of pressure, temperature and displacement gradients evaluated at the interface. For boundary interfaces, we employ a single-side approximation of those gradients, i.e. $\boldsymbol{\xi}_\tau = \boldsymbol{\xi}_{1\tau}$. For interior interfaces, we utilize the following weighting

$$\boldsymbol{\xi}_\tau = \frac{\boldsymbol{\xi}_{\tau 1} + \boldsymbol{\xi}_{\tau 2}}{2}, \tag{32}$$

A set of cells that contribute to the approximation Eq. (32) for each interface of some cell j is illustrated in Fig. 1.

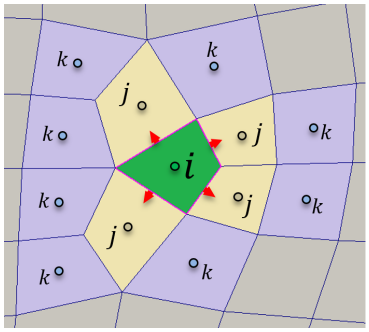

Figure 1: Cells that contribute to the approximation of fluxes over the interfaces of cell i. Index j denotes the nearest neighbors of cell i. Index k denotes farther neighbors that contribute to the gradients reconstructed in cells j.

It is worth mentioning that the least squares solution in Eq. (29) allows computing the gradients of unknowns locally and independently for every cell. Note, however, that it does not guarantee the local conservation property for the scheme. In order to maintain it, individual gradients for every interface that respects the corresponding flux balance should be employed.

Solution strategy

Solving the system of $n_c + 4$ nonlinear discrete equations written in Eq. (19) involves significant computational challenges. We utilize Newton-Raphson iterations to resolve nonlinearities. Linear systems appearing in these iterations can not be efficiently handled with direct solvers already for grids comprised of 10^4 cells. Therefore, the scalable iterative linear solution strategy is required for the integration of realistic models ($\gtrsim 10^4$ cells).

In this work, we implement the two-stage block-partitioned preconditioning strategy for multiphase poromechanics (White et al., 2019). The strategy exploits the fixed-stress approximation, which has been initially developed for the sequential solution of poromechanical systems (Kim et al., 2011), and later has been successfully utilized in the preconditioning of fully implicit systems (White et al., 2016).

In the first stage, this preconditioning strategy considers the block-partitioned system

$$\mathbf{U}^{-1}\mathbf{J}\boldsymbol{\delta}\mathbf{d} = \begin{bmatrix} \mathbf{I} & \mathbf{0} & -\mathbf{J}_{pu}\mathbf{J}_{uu}^{-1} \\ \mathbf{0} & \mathbf{I} & -\mathbf{J}_{su}\mathbf{J}_{uu}^{-1} \\ 0 & 0 & \mathbf{I} \end{bmatrix} \left[\begin{array}{cc|c} \mathbf{J}_{pp} & \mathbf{J}_{ps} & \mathbf{J}_{pu} \\ \mathbf{J}_{sp} & \mathbf{J}_{ss} & \mathbf{J}_{su} \\ \hline \mathbf{J}_{up} & \mathbf{J}_{us} & \mathbf{J}_{uu} \end{array}\right] \begin{bmatrix} \boldsymbol{\delta}\mathbf{p} \\ \boldsymbol{\delta}\mathbf{s} \\ \boldsymbol{\delta}\mathbf{u} \end{bmatrix} =$$

$$= \left[\begin{array}{cc|c} \multicolumn{2}{c|}{\multirow{2}{*}{$\mathbf{S}_{ps}$}} & \mathbf{0} \\ & & \mathbf{0} \\ \hline \mathbf{J}_{up} & \mathbf{J}_{us} & \mathbf{J}_{uu} \end{array}\right] \begin{bmatrix} \boldsymbol{\delta}\mathbf{p} \\ \boldsymbol{\delta}\mathbf{s} \\ \boldsymbol{\delta}\mathbf{u} \end{bmatrix} = - \begin{bmatrix} \mathbf{H}_p - \mathbf{J}_{pu}\mathbf{J}_{uu}^{-1}\mathbf{H}_u \\ \mathbf{H}_s - \mathbf{J}_{su}\mathbf{J}_{uu}^{-1}\mathbf{H}_u \\ \mathbf{H}_u \end{bmatrix}, \quad (33)$$

where $\mathbf{J}$ is the Jacobian matrix, $\boldsymbol{\delta}\mathbf{d} = [\boldsymbol{\delta}\mathbf{p}, \boldsymbol{\delta}\mathbf{s}, \boldsymbol{\delta}\mathbf{u}]^T$ is the vector of unknown increments of pressures, compositions (and temperature for non-isothermal systems) and displacements while $\mathbf{H}_p, \mathbf{H}_s$ and $\mathbf{H}_u$ are the residuals in corresponding equations. The Schur complement $\mathbf{S}_{ps}$ of block $\mathbf{J}_{uu}$ in the Jacobian is equal to

$$\mathbf{S}_{ps} = \begin{bmatrix} \mathbf{J}_{pp} - \mathbf{J}_{pu}\mathbf{J}_{uu}^{-1}\mathbf{J}_{up} & \mathbf{J}_{ps} - \mathbf{J}_{pu}\mathbf{J}_{uu}^{-1}\mathbf{J}_{us} \\ \mathbf{J}_{sp} - \mathbf{J}_{su}\mathbf{J}_{uu}^{-1}\mathbf{J}_{up} & \mathbf{J}_{ss} - \mathbf{J}_{su}\mathbf{J}_{uu}^{-1}\mathbf{J}_{us} \end{bmatrix}, \quad (34)$$

and can be approximated by $\tilde{\mathbf{S}}_{ps}$ defined as

$$\tilde{\mathbf{S}}_{ps} = \begin{bmatrix} \mathbf{J}_{pp} - \mathrm{diag}\left(\mathbf{J}_{pu}\mathbf{J}_{uu}^{-1}\mathbf{J}_{up}\mathbf{e}\right) & \mathbf{J}_{ps} \\ \mathbf{J}_{sp} - \mathrm{diag}\left(\mathbf{J}_{su}\mathbf{J}_{uu}^{-1}\mathbf{J}_{up}\mathbf{e}\right) & \mathbf{J}_{ss} \end{bmatrix}, \quad (35)$$

where row-sum lumping strategy is utilized (Klevtsov et al., 2016), $\mathbf{e} = [1, \cdots, 1]^T$ is a probing vector and diag() denotes a diagonal matrix constructed from an input vector. For the evaluation of $\mathbf{J}_{uu}^{-1}$ we use a single V-cycle of algebraic multigrid (AMG) solver that provides a good approximation to this matrix.

In the second stage, the Constrained Pressure Residual (CPR) preconditioner (Wallis et al., 1985; Cao et al., 2005) can be used to find an approximate solution for the multiphase flow system. CPR preconditioner also performs in two stages. In the first stage, the system is divided into pressure (elliptic) and composition (hyperbolic) subsystems with True-IMPES (implicit-pressure explicit-saturation) reduction algorithm (K. Aziz, 1979). The pressure subsystem is solved with an AMG solver and often a single V-cycle provides a precise enough solution. In the second stage of the CPR preconditioner, the multiphase flow system with substituted pressure solution is subjected to the Incomplete LU (ILU) preconditioner. The described CPR preconditioner has proven to be robust and efficient in accelerating the modeling of a wide range of geo-energy applications (Cao et al., 2005; Khait et al., 2020) Further improvement of CPR preconditioner in the presence of heat conduction is possible (Roy et al., 2020; Cremon et al., 2024).

Results

Convergence study

Convergence study of the system of Eqs. (1)-(3) is complicated by a few nonlinearities. First, it is possible to investigate convergence only for single-phase slightly compressible flow as multiphase compositional flow introduces unavoidable nonlinearities compromising the measurement of convergence rate. Second, the effective density, internal energy and heat conduction averaged over fluid and rock matrix introduce additional nonlinearities in the system. For this study, we simplify these terms as

$$(1-\phi)\rho_s + \phi\sum_{\alpha}^{\mathrm{n}_p} \mathrm{s}_\alpha\rho_\alpha \to \rho_{\mathrm{tot}}, \quad (36)$$

$$(1-\phi)\rho_s\mathrm{U}_s + \phi\sum_{\alpha}^{\mathrm{n}_p} \mathrm{s}_\alpha\rho_\alpha\mathrm{U}_s \to \mathrm{h}_{\mathrm{tot}} = \mathrm{cT}, \quad (37)$$

$$(1-\phi)\mathbf{q}_s^{(\theta)} + \sum_{\alpha}^{\mathrm{n}_p} \phi\mathrm{s}_\alpha\mathbf{q}_\alpha^{(\theta)} \to \mathbf{q}_{\mathrm{tot}}^{(\theta)} = -\boldsymbol{\Lambda}\nabla\mathrm{T}, \quad (38)$$

where ρ_{tot} is a constant, h_{tot} and the approximated $\mathbf{q}_{\text{tot}}^{(\theta)}$ are linear functions of unknowns, with constant heat capacity c and heat conductivity tensor $\mathbf{\Lambda}$. Note that Eq. (37) neglects the thermoporoelastic effect on temperature through porosity changes with alternating pressure and temperature.

Despite these simplifications, the heat convection in Eq. (2) maintains the system nonlinear. To overcome this nonlinearity, we perform two convergence studies: the first one investigates the convergence of a poroelastic system without energy balance while the second, thermoporoelastic, one considers a linear pressure distribution which allows the convergence of the system to be estimated in the presence of heat convection. The linearity-preserving property of these numerical schemes (Terekhov, 2020; Novikov et al., 2022) enables the machine-precision approximation of linearly distributed unknowns across a domain. As a result, Darcy's fluxes enjoy a much more accurate approximation compared to the enthalpy multiplier defined by nonlinearly distributed temperature across the domain. This explains the possibility of measuring the convergence rate in the second study.

Consider a cubic domain $\Omega = [0,1]^3$ [m] with the following constant stiffness matrix $\mathbf{C}$, Biot tensor $\mathbf{B}$, permeability tensor $\mathbf{K}$, thermal dilation tensor $\mathbf{A}$ and heat conductivity tensor $\mathbf{\Lambda}$:

$$\mathbf{C} = \begin{bmatrix} 1.323 & 0.0726 & 0.263 & 0.108 & -0.08 & -0.239 \\ 0.0726 & 1.276 & -0.318 & 0.383 & 0.108 & 0.501 \\ 0.263 & -0.318 & 0.943 & -0.183 & 0.146 & 0.182 \\ 0.108 & 0.383 & -0.183 & 1.517 & -0.0127 & -0.304 \\ -0.08 & 0.108 & 0.146 & -0.0127 & 1.209 & -0.326 \\ -0.239 & 0.501 & 0.182 & -0.304 & -0.326 & 1.373 \end{bmatrix} [\text{bar}], \tag{39}$$

$$\mathbf{B} = \begin{bmatrix} 1.5 & 0.1 & 0.5 \\ 0.1 & 1.5 & 0.15 \\ 0.5 & 0.15 & 1.5 \end{bmatrix}, \qquad \mathbf{K} = \begin{bmatrix} 1.5 & 0.5 & 0.35 \\ 0.5 & 1.5 & 0.45 \\ 0.35 & 0.45 & 1.5 \end{bmatrix} [\text{mD}], \tag{40}$$

$$\mathbf{A} = \begin{bmatrix} 1.5 & 0.5 & 0.35 \\ 0.5 & 1.5 & 0.45 \\ 0.35 & 0.45 & 1.5 \end{bmatrix} [\text{bar}\,\text{K}^{-1}], \qquad \mathbf{\Lambda} = \alpha \begin{bmatrix} 1.5 & 0.1 & 0.5 \\ 0.1 & 1.5 & 0.15 \\ 0.5 & 0.15 & 1.5 \end{bmatrix} [\text{J}\,\text{d}^{-1}\,\text{m}^{-1}\,\text{K}^{-1}], \tag{41}$$

where α denotes an input parameter used to measure the convergence rate for various Peclet numbers. The remaining properties are listed in Tab. 1.

Table 1: The remaining properties used in the convergence studies.

Property	Value	Unit
Porosity, ϕ_0	0.1	-
Fluid density, ρ_{f}	978	$\text{kg}\,\text{m}^{-3}$
Fluid viscosity, μ_{f}	0.01	cP
Fluid compressibility, β_{f}	0	bar^{-1}
Total density, ρ_{tot}	2482.8	$\text{kg}\,\text{m}^{-3}$
Rock compressibility, β_s	1.4503768×10^{-6}	bar^{-1}
Gravitational acceleration, g	0.0981	$\text{m}\,\text{d}^{-2}$
Heat capacity, c	1	$\text{kJ}\,\text{m}^{-3}\,\text{K}^{-1}$

Let us consider the reference solution for displacements defined as

$$\begin{aligned} u(x,y,z,t) &= \left[(x-0.5)^2 - y - z\right](1+t^2), \\ v(x,y,z,t) &= \left[(y-0.5)^2 - x - z\right](1+t^2), \\ w(x,y,z,t) &= \left[(z-0.5)^2 - x - y\right](1+t^2). \end{aligned} \tag{42}$$

Additionally, let us define the following nonlinear function

$$f(x,y,z,t) = \frac{1}{2\sin(1)} \sin((1-x)(1-y)(1-z)) + 0.5(1-x)^3(1-y)^2(1-z)(1+t^2). \tag{43}$$

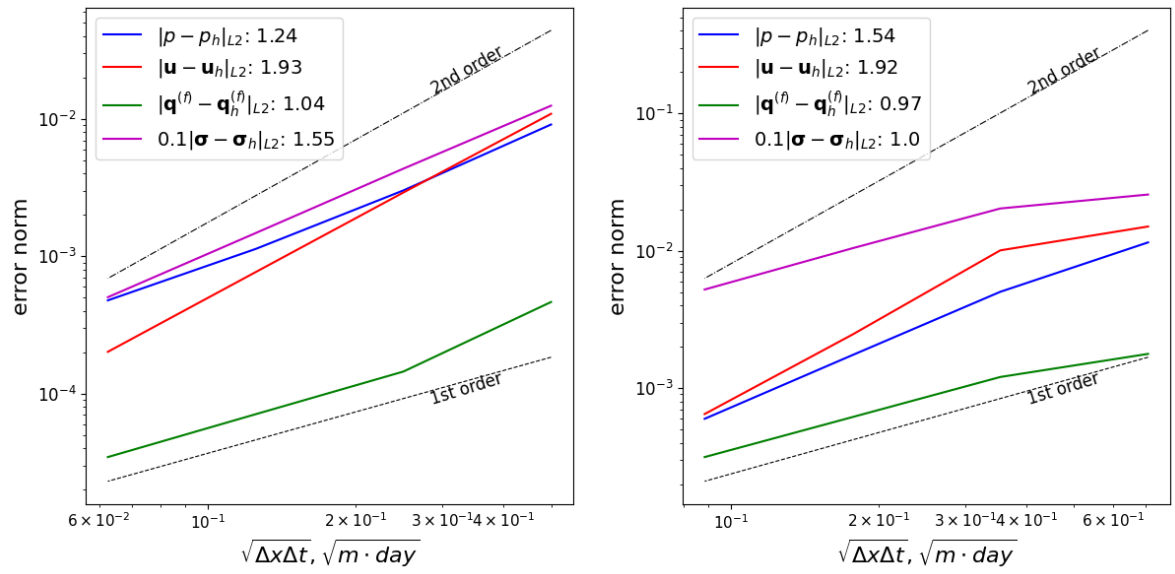

(a) cubic grid

(b) tetrahedral grid

Figure 2: The L2 error norm against space-time resolution obtained with cubic (a) and tetrahedral (a) grids.

In the first convergence study, we estimate the convergence rate for the poroelastic system. For this purpose we utilize the function from Eq. (43) as a pressure reference solution, i.e. $\mathrm{p} = f$. Neither energy balance nor thermal dilation are considered in this study. Subsequently, the reference displacement and pressure solutions are substituted to fluid mass and momentum balance Eqs. (1) and (3); and the respective right-hand sides of these equations are calculated for every cell at every time step. These values are substituted to the numerical scheme as free terms. Besides, the reference solution defines Dirichlet boundary conditions, applied to fluid and momentum balance equations. As a result, the numerical scheme must approximate the given reference solution.

Fig. 2 demonstrates the L2 error norms between reference $\mathrm{p}, \mathbf{u}$ and numerical $\mathrm{p}_h, \mathbf{u}_h$ solutions against spatiotemporal resolution. The results are obtained with a series of cubic and tetrahedral grids composed of 8^2, 8^3, 8^4, 8^5 cubes and 100, 384, 2604, 18921 tetrahedrons, respectively. As it was shown before (Terekhov, 2020; Novikov et al., 2022), displacements demonstrate a nearly quadratic convergence rate while pressure, which suffers from the first-order approximation of time derivatives, exhibits only a super-linear convergence rate. Additionally, Fig. 2 illustrates a linear convergence rate of Darcy's velocities $\mathrm{q}_h^{(\mathrm{f})}$ and stress tensors $\boldsymbol{\sigma}_h$ reconstructed at cell centers.

In the second convergence study, we estimate the convergence rate for the thermoporoelastic system. To avoid the nonlinearity of convective fluxes in energy balance, we employ the following time-independent reference solution for pressure

$$p(x,y,z,t) = 3 - x - y - z, \tag{44}$$

which represents a linear function in space. Temperature is defined by the reference solution from Eq. (43), i.e. $\mathrm{T} = f$ while the reference solutions for displacements remain the one defined in Eq. (42). Following the same procedure as in the first study, we incorporate these reference solutions into the numerical calculations.

Thermoporoelastic extension of SPE10 model

This field-scale test case utilizes a reservoir model from the 10th SPE Comparative Solution Project (SPE10). Following Garipov et al. (2018), we extend this model with mechanical properties to perform coupled THMC modeling.

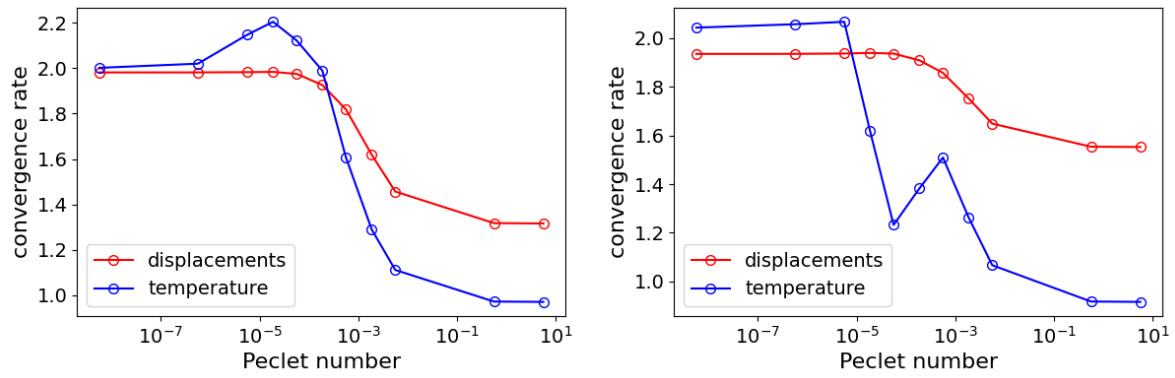

(a) cubic grid

(b) tetrahedral grid

Figure 3: The sensitivity of numerical convergence rate to the Peclet number of heat transfer investigated with cubic (a) and tetrahedral (a) grids.

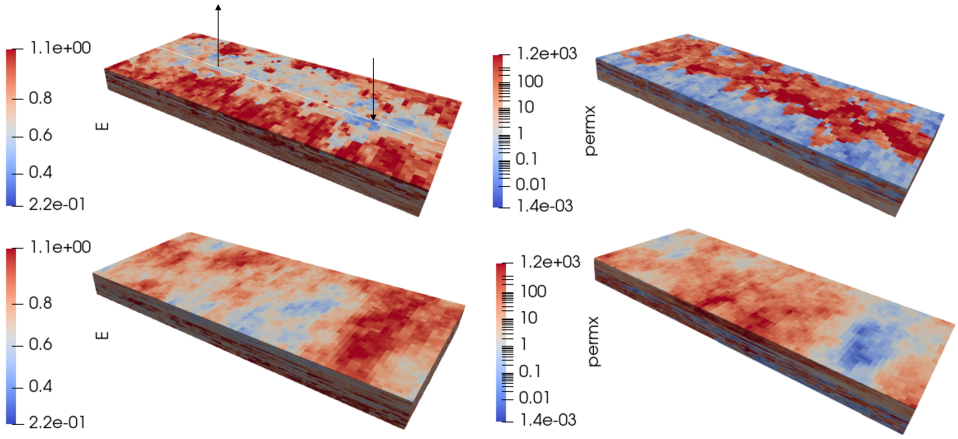

Figure 4: Young modulus (in tens of GPa) and lateral permeability (in mD) fields shown from the top (top row) and from the bottom (bottom row) of reservoir. Young's modulus is calculated as a linear function of porosity.

The original project's model is covered with a regular Cartesian $60 \times 220 \times 85$ grid that spans two formations: the top 50 layers have a channelized permeability distribution while the bottom 35 layers represent a permeability field that has a Gaussian spatial covariance. Mechanical properties are defined by heterogeneous Young's modulus linearly dependent on porosity, uniform Poisson's ratio $\nu = 0.2$, Biot's coefficient $b = 1$, thermal expansion coefficient $\alpha = 9 \cdot 10^{-7} {}^{\circ}\mathrm{C}^{-1}$. The reservoir has a uniform rock density $\rho_s = 2650\,\mathrm{kg\,m^{-3}}$, rock heat capacity $\mathrm{c}_s = 2.2\,\mathrm{kJ\,kg^{-1}\,{}^{\circ}C^{-1}}$ and effective heat conductivity $\lambda_0 = 72.23\,\mathrm{kJ\,m^{-1}\,d^{-1}\,{}^{\circ}C^{-1}}$. Fig. 4 shows the corresponding Young's modulus E and x-axis permeability k_x maps. For the scalability study, we coarsened the original model using a volume-averaging approach (Garipov et al., 2018). The domain is subjected to impermeable boundary conditions and constant temperature defined by the temperature at top $\mathrm{T_{top}} = 26.85\,{}^{\circ}\mathrm{C}$ and bottom $\mathrm{T_{bot}} = 76.85\,{}^{\circ}\mathrm{C}$ of domain distributed between according to a constant geothermal gradient. Furthermore, we apply roller boundary conditions at all domain's sides except the top boundary where we apply a uniform normal load $\mathrm{f}_N^{\mathrm{top}} = 90\,\mathrm{MPa}$.

In this study, we examine three fluid physics: single-phase, two-phase and thermal two-phase. Tab. 2 list parameters which describe single-phase and thermal two-phase fluid physics. For the isothermal two-phase fluid physics, thermal properties should be omitted.

We model the THMC reservoir response perturbed by the doublet of injection and production wells placed over the longest centerline (along the y-axis) as shown in the top-left of Fig. 4. The vertical wells

Table 2: The description of fluid physics used in the study.

Property	Single-phase	Two-phase
Phase densities, $\mathrm{kg\,m^{-3}}$	666.85	1014, 50
Phase compressibilities, $\mathrm{bar^{-1}}$	$1.45 \cdot 10^{-5}$	$10^{-5}, 5 \cdot 10^{-3}$
Phase viscosities, cP	1.0	0.3, 0.03
Connate water saturations	–	0.1, 0.1
Residual gas saturation	–	0.1, 0.1
Corey exponent	–	2
Phase heat capacities, $\mathrm{kJ\,kg^{-1}\,^{\circ}C^{-1}}$	–	4.18, 0.035
Initial phase saturation	1	0.67, 0.33

perforate the whole thickness of the reservoir. Pressure controls $\mathrm{p}_{inj} = \mathrm{p}_{\max} + 50\,\mathrm{bar}$ and $\mathrm{p}_{\mathrm{prod}} = \mathrm{p}_{\min} - 50\,\mathrm{bar}$ are applied to the wells, respectively, where $\mathrm{p}_{\max}$ and $\mathrm{p}_{\min}$ are maximal and minimal unperturbed pressures over perforated cells. In all variants of fluid physics, single-phase fluid is pumped into the reservoir through the injection well. In the case of two-phase thermal fluid, specifically, pure water of temperature $\mathrm{T}_{\mathrm{inj}} = 27.85\,^{\circ}\mathrm{C}$ is injected. The simulation is performed up to $t_{\max} = 20\,\mathrm{d}$.

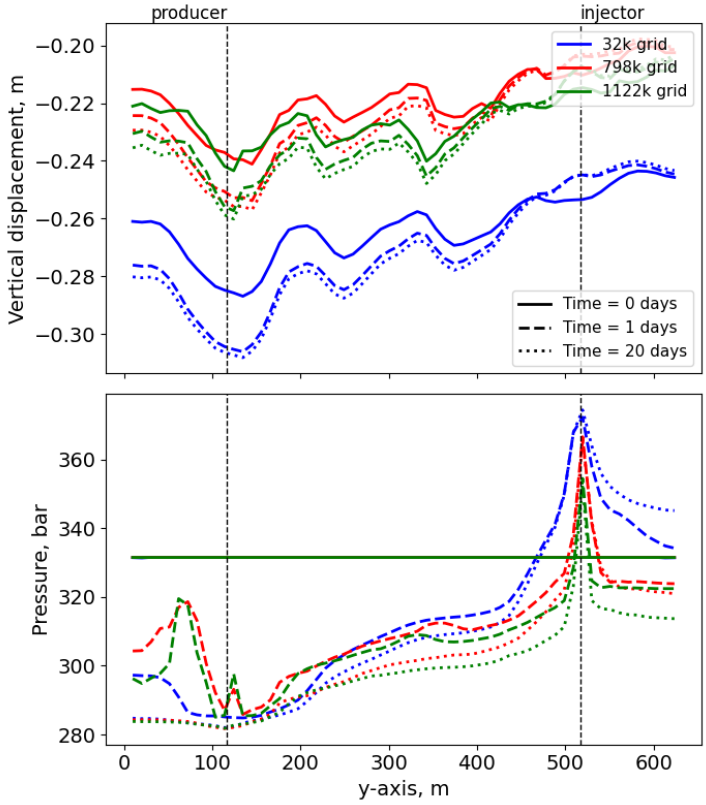

Figure 5: Solution profiles for single-phase fluid plotted over the longest centerline at the top of the reservoir (white line in the top-left of Fig. 4). The results are displayed for three different grid resolutions and at three time steps.

Figs. 5 and 6 demonstrate solution profiles along the longest centerline of the reservoir, indicated by a white line in the top-left of Fig. 4. This centerline passes through the top of the reservoir and is aligned with the y-axis. Fig. 5 presents the vertical displacement and pressure obtained for single-phase fluid while Fig. 6 additionally shows water saturation and water saturation with temperature obtained for two-phase and thermal two-phase fluids, respectively. The results for three different grid resolutions and at three time steps $t = 0, 1, 20\,\mathrm{d}$ are shown in both figures.

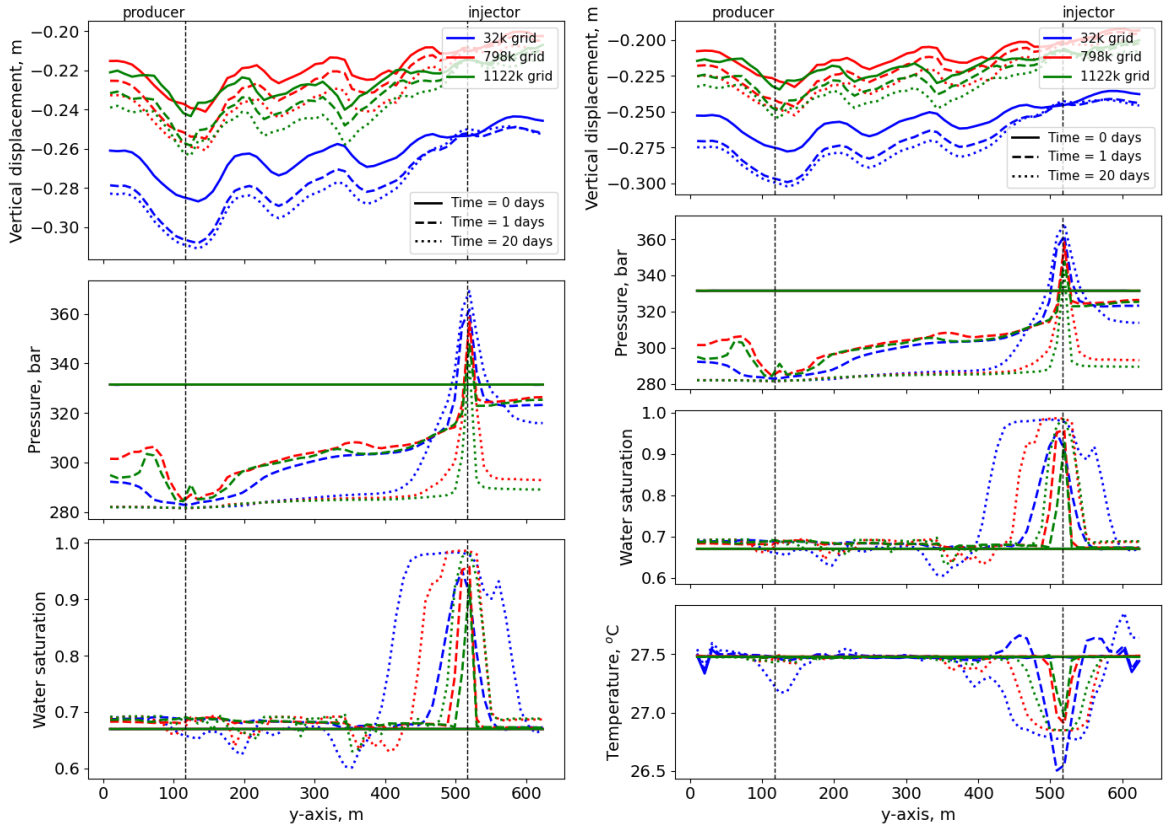

(a) Two-phase fluid

(b) Thermal two-phase fluid

Figure 6: Solution profiles for two-phase (a) and thermal two-phase (b) fluids plotted over the longest centerline at the top of the reservoir (white line in the top-left of Fig. 4). The results are displayed for three different grid resolutions and at three time steps.

The vertical displacement profiles for all three fluid types show significant differences between grid resolutions. The results calculated with the coarsest resolution (32k) overestimate subsidence compared to those calculated with finer grids. This applies to both the subsidence at the initial unperturbed condition ($t = 0\,\mathrm{d}$) and the subsidence due to well operation ($t = 20\,\mathrm{d}$). The major contribution to this difference in vertical displacement can be attributed to the varying stiffness heterogeneities specified for different grid resolutions. Additionally, this difference can be partly explained by the difference in pressures obtained for different grid resolutions. Indeed, the pressure spike around the injection well is localized in a narrower region on the finer grids compared to the coarser grid. Besides, the narrower pressure spike around the injection well for finer grids explains the shorter propagation of water saturation and temperature fronts.

Efficient modeling of THMC processes in realistic settings requires a scalable computational framework. Figure 7 presents the results of the scalability study of the implemented block-partitioned preconditioner. It shows the number of linear and nonlinear iterations needed to obtain convergent solutions in 20 timesteps for various grid resolutions. The model heterogeneities are upscaled from the original SPE10 dataset provided at the finest grid resolution. The results indicate a linear increase in the number of linear iterations with increasing grid size, which suggests weak scalability of the linear solver.

For the same model runs, Fig. 8 presents the cummulative runtime of the block-partitioned preconditioner. Additionally, the runtime of the setup and solve calls are specified. Both setup and solve calls are executed at every iteration of the linear solver (GMRES). The setup call performs the approximation of Schur complement $\tilde{\mathbf{S}}_{ps}$, including the setup of AMG preconditioners for pressure $\mathbf{J}_{pp}$ and displacement $\mathbf{J}_{uu}$ subsystems. Note, that under linear thermo-poroelastic assumption and the boundary conditions of

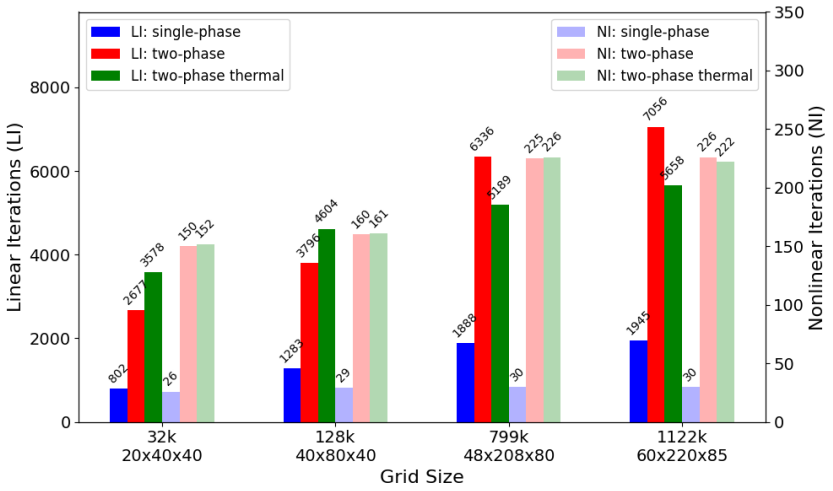

Figure 7: Scalability study of the block-partitioned preconditioner. The cumulative number of linear (left axis) and nonlinear (right axis) iterations required to achieve convergent solutions in 20 timesteps is plotted against multiple grid resolutions.

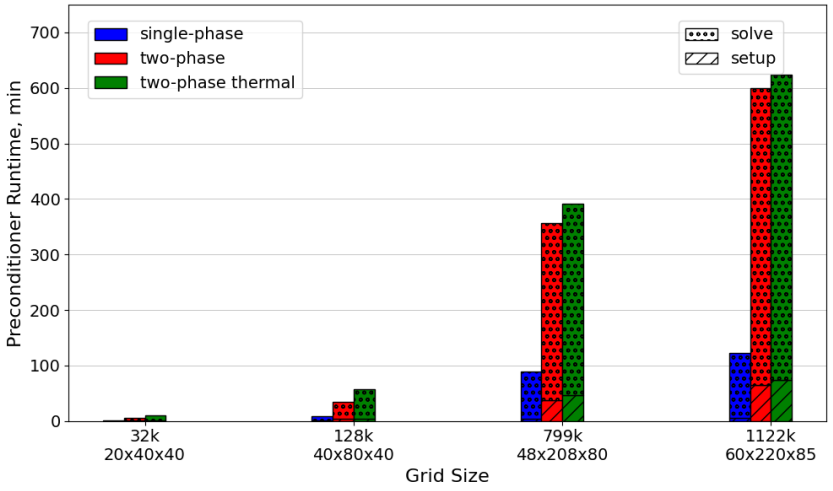

Figure 8: Cummulative runtime of the block-partitioned preconditioner to achieve convergent solutions in 20 timesteps. Timings of setup and solve calls are provided.

the same type, the latter is not needed as $\mathbf{J}_{uu}$ remains constant over iterations and timesteps. The solve call performs the solution of flow and, subsequently, displacement subsystems. Although, the setup includes redundant setup of AMG preconditioner for displacement subsystem, it constitutes a small part (<15%) of preconditioner's runtime. Most of the runtime is taken by solve call, specifically solve of displacement subsystem. The increase in the preconditioner's runtime is almost linear which again indicates weak scalability of the preconditioner.

Heat conduction terms introduce additional elliptic terms that are not treated efficiently at the CPR stage of the block-partitioned preconditioner. Fig. 9 demonstrates the sensitivity of solving performance to the magnitude of heat conduction term. It shows the number of linear and nonlinear iterations needed to obtain convergent solutions in 20 timesteps for multiple values of effective heat conduction coefficient. The figure shows an insignificant increase in linear iterations with higher heat conduction coefficient, for the values of heat conduction between $10^{-4}\lambda_0$ and $10^{2}\lambda_0$. This almost flat behavior might be explained by an already high number of iterations spent by the block-partitioned preconditioner. In the case of extremely high heat conduction, we observe a significant increase in the number of linear iterations, as anticipated.

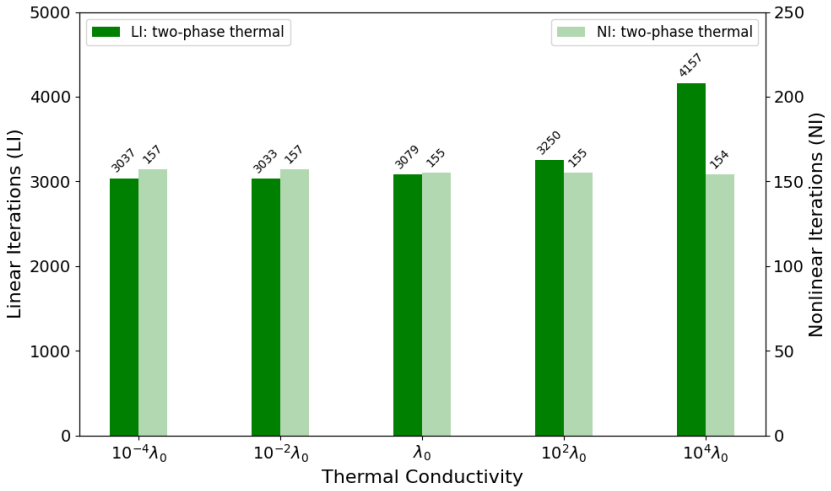

Figure 9: Sensitivity of linear (left axis) and nonlinear (right axis) iterations to the effective thermal conductivity. Calculations are performed using $24 \times 104 \times 40$ grid with thermal two-phase fluid physics.

Conclusion

In this paper, we have introduced a novel cell-centered collocated fully implicit scheme of the Finite Volume Method (FVM) for the coupled modeling of thermo-hydro-mechanical-compositional processes in thermoporoelastic rocks. The scheme benefits from the vectorized form of mass, energy and momentum fluxes, obtained with multi-point approximations, that simplifies multiphysical simulation within FVM. Furthermore, the use of collocated FVM for momentum balance enables the natural integration of thermal composition flow with geomechanics within a single computational grid and engine. Additionally, we implemented a block-partitioned preconditioning strategy that alleviates the costs of fully implicit coupling and enables efficient modeling of large realistic setups.

The proposed framework has been validated using a simplified version of the physics which allows us to use an analytic convergence benchmark. We show that in the poroelastic case, the displacements exhibit a nearly quadratic convergence rate while pressure demonstrates a super-linear convergence. In the thermo-poroelastic case, the convergence rate changes from quadratic to lower orders depending on the thermal Peclet number. We also demonstrate how the performance of the full multiphase THMC model depends on the grid resolution using the mechanical extension of the SPE10 model. Future work would include better tuning of the preconditioner, offloading assembly and solvers to GPU to further minimize computational costs of modeling, and the support of faults with frictional contacts to enable modeling of fault reactivation.

Acknowledgements

A part of this work was performed in the *Science4Steer* project (DEEP.NL.2018.046) financed by the Dutch Research Council (NWO). Additional funding comes from NWO (grant number 18816) and TotalEnergies (FC-MAELSTROM Project).

Nomenclature

Physical variables

A – rank-two rock thermal dilation tensor,
α_ϕ – volumetric thermal dilation coefficient related to porosity
B – rank-two Biot tensor,
$\mathbb{C}$ – rank-four stiffness tensor of skeleton,

$\mathbf{C}$ – 6×6 matrix of stiffness coefficients,
c_α – heat capacity of fluid phase α,
c_s – rock heat capacity,
$\boldsymbol{\varepsilon}$ – rank-two infinitesimal strain tensor,
E – Young's modulus,
$\mathbf{f}$ – traction vector,
$f_N, \mathbf{f}_T$ – normal and tangential projections of traction vector,
G – shear modulus,
g – gravity constant,
h_f – fluid enthalpy,
$\mathbf{I}$ – identity matrix,
$\mathbf{K}$ – rank-two tensor of permeability,
k_x, k_y, k_z – diagonal components of permeability tensor,
$k_{r\alpha}$ – relative permeability of fluid phase f,
K_r – bulk modulus of the solid phase,
$\boldsymbol{\Lambda}$ – rank-two effective heat conductivity tensor,
μ_α – fluid viscosity of fluid phase α,
$\mathbf{n}$ – unit normal vector,
ν – Poisson's ratio,
p – pore pressure,
$\mathbf{q}_\alpha^{(f)}$ – Darcy's velocity of fluid phase f,
$\mathbf{q}_\alpha^{(\theta)}$ – heat conduction vector fluid constituent α (fluid phase of rock),
r_α – sources (or sinks) of fluid mass of phase α,
ρ_α – density of constituent α,
s_α – saturation of fluid phase α,
$\boldsymbol{\sigma}$ – rank-two total stress tensor,
T – temperature,
t – time,
U_f – fluid internal energy,
U_r – rock internal energy,
$\mathbf{u} = [u_x\, u_y\, u_z]^T$ – vector of displacements,
$(\nabla \mathbf{u})^T$ – Jacobian matrix of $\mathbf{u}$,
ϕ – porosity,
$\tilde{\phi} = \phi_0 + (p - p_0)(\psi - \phi_0)/K_r$,
$\psi = (\mathbf{B} : \mathbf{I})\,/\,3$ – one-third of the trace of tensor $\mathbf{B}$,
$x_{i\alpha}$ – molar fraction of component i in fluid phase α,
z – depth.

Numerical variables

Δt – time step,
δ_j – area of jth interface,
$\mathbf{H}$ – vector of residuals,
$\mathbf{J}$ – Jacobian matrix,
$\boldsymbol{\delta}\mathbf{p}, \boldsymbol{\delta}\mathbf{s}, \boldsymbol{\delta}\mathbf{u}$ – unknown increments of pressures,
$\boldsymbol{\delta}\mathbf{s}$ – unknown increments of compositions (and temperatures for non-isothermal systems),
$\boldsymbol{\delta}\mathbf{u}$ – unknown increments of displacements.

References

Aavatsmark, I., Barkve, T., Boe, O. and Mannseth, T. [1996] Discretization on Non-Orthogonal, Quadrilateral Grids for Inhomogeneous, Anisotropic Media. *Journal of Computational Physics*, **127**(1), 2–14.

Bai, B. [2005] One-dimensional thermal consolidation characteristics of geotechnical media under non-isothermal condition. *Gongcheng Lixue/Engineering Mechanics*, **22**, 186–191.

Berge, R., Berre, I., Keilegavlen, E., Nordbotten, J. and Wohlmuth, B. [2020] Finite volume discretization for poroelastic media with fractures modeled by contact mechanics. *International Journal for Numerical Methods in Engineering*, **121**(4), 644–663.

Buijze, L., Guo, Y., Niemeijer, A., Ma, S. and Spiers, C. [2020] Nucleation of Stick-Slip Instability Within a Large-Scale Experimental Fault: Effects of Stress Heterogeneities Due to Loading and Gouge Layer Compaction. *Journal of Geophysical Research: Solid Earth*, **125**(8).

Cao, H., Tchelepi, H., Wallis, J. and Yardumian, H. [2005] Parallel scalable unstructured CPR-type linear solver for reservoir simulation. 3319 – 3326.

Cheng, A.D. [1997] Material coefficients of anisotropic poroelasticity. *International journal of rock mechanics and mining sciences & geomechanics abstracts*, **34**(2), 199–205.

Cheng, Y., Liu, W., Xu, T., Zhang, Y., Zhang, X., Xing, Y., Feng, B. and Xia, Y. [2023] Seismicity induced by geological CO2 storage: A review. *Earth-Science Reviews*, **239**.

Coussy, O. [2003] *Thermoporoelasticity*, chap. 4. John Wiley & Sons, Ltd, 71–112.

Cremon, M.A., Franc, J. and Hamon, F.P. [2024] Constrained pressure-temperature residual (CPTR) preconditioner performance for large-scale thermal CO2 injection simulation. *Computational Geosciences*.

Deb, R. and Jenny, P. [2017a] Finite volume–based modeling of flow-induced shear failure along fracture manifolds. *International Journal for Numerical and Analytical Methods in Geomechanics*, **41**(18), 1922–1942.

Deb, R. and Jenny, P. [2017b] Modeling of shear failure in fractured reservoirs with a porous matrix. *Computational Geosciences*, **21**(5-6), 1119–1134.

Dost, B., Ruigrok, E. and Spetzler, J. [2017] Development of seismicity and probabilistic hazard assessment for the Groningen gas field. *Geologie en Mijnbouw/Netherlands Journal of Geosciences*, **96**(5), s235 – s245.

Edwards, M.G. and Rogers, C.F. [1998] Finite volume discretization with imposed flux continuity for the general tensor pressure equation. *Computational Geosciences*, **2**, 259–290.

Ellsworth, W.L., Giardini, D., Townend, J., Ge, S. and Shimamoto, T. [2019] Triggering of the Pohang, Korea, Earthquake (Mw 5.5) by enhanced geothermal system stimulation. *Seismological Research Letters*, **90**(5), 1844 – 1858.

Gao, Q. and Ghassemi, A. [2020] Three-Dimensional Thermo-Poroelastic Modeling and Analysis of Flow, Heat Transport and Deformation in Fractured Rock with Applications to a Lab-Scale Geothermal System. *Rock Mechanics and Rock Engineering*, **53**, 1–22.

Garipov, T. and Hui, M. [2019] Discrete Fracture Modeling approach for simulating coupled thermo-hydro-mechanical effects in fractured reservoirs. *International Journal of Rock Mechanics and Mining Sciences*, **122**.

Garipov, T., Karimi-Fard, M. and Tchelepi, H. [2016] Discrete fracture model for coupled flow and geomechanics. *Computational Geosciences*, **20**(1), 149–160.

Garipov, T., Tomin, P., Rin, R., Voskov, D. and Tchelepi, H. [2018] Unified thermo-compositional-mechanical framework for reservoir simulation. *Computational Geosciences*, **22**(4), 1039–1057.

Henson, V.E. and Yang, U.M. [2002] BoomerAMG: A parallel algebraic multigrid solver and preconditioner. *Applied Numerical Mathematics*, **41**(1), 155 – 177.

K. Aziz, A.S. [1979] *Petroleum Reservoir Simulation*. Applied Science Publishers LTD.

Kala, K. and Voskov, D. [2020] Element balance formulation in reactive compositional flow and transport with parameterization technique. *Computational Geosciences*, **24**(2), 609–624.

Keilegavlen, E. and Aavatsmark, I. [2008] Monotonicity for control volume methods on unstructured grids.

Khait, M. and Voskov, D. [2018a] Adaptive parameterization for solving of thermal/compositional nonlinear flow and transport with buoyancy. *SPE Journal*, **23**(2), 522–534.

Khait, M. and Voskov, D. [2018b] Operator-based linearization for efficient modeling of geothermal

processes. *Geothermics*, **74**, 7–18.
Khait, M., Voskov, D. and Zaydullin, R. [2020] High performance framework for modelling of complex subsurface flow and transport applications.
Khait, M. and Voskov, D.V. [2017] Operator-based linearization for general purpose reservoir simulation. *Journal of Petroleum Science and Engineering*, **157**, 990 – 998.
Kim, J., Tchelepi, H. and Juanes, R. [2011] Stability and convergence of sequential methods for coupled flow and geomechanics: Fixed-stress and fixed-strain splits. *Computer Methods in Applied Mechanics and Engineering*, **200**(13-16), 1591–1606.
Klevtsov, S., Castelletto, N., White, J. and Tchelepi, H. [2016] Block-preconditioned krylov methods for coupled multiphase reservoir flow and geomechanics.
Le Potier, C. [2005] Finite volume monotone scheme for highly anisotropic diffusion operators on unstructured triangular meshes; [Schéma volumes finis monotone pour des opérateurs de diffusion fortement anisotropes sur des maillages de triangles non structurés]. *Comptes Rendus Mathematique*, **341**(12), 787 – 792.
Lyu, X., Khait, M. and Voskov, D. [2021a] Operator-based linearization approach for modeling of multiphase flow with buoyancy and capillarity. *SPE Journal*, **26**(4), 1858–1878.
Lyu, X., Voskov, D. and Rossen, W. [2021b] Numerical investigations of foam-assisted CO2 storage in saline aquifers. *International Journal of Greenhouse Gas Control*, **108**.
Nardean, S., Ferronato, M. and Abushaikha, A. [2022] Linear Solvers for Reservoir Simulation Problems: An Overview and Recent Developments. *Archives of Computational Methods in Engineering*, **29**(6), 4341 – 4378.
Nordbotten, J.M. [2014] Cell-centered finite volume discretizations for deformable porous media. *International Journal for Numerical Methods in Engineering*, **100**(6), 399–418.
Nordbotten, J.M. [2016] Stable cell-centered finite volume discretization for biot equations. *SIAM Journal on Numerical Analysis*, **54**(2), 942 – 968.
Novikov, A. [2024] *A Finite Volume Framework for Accurate Modeling of Fault Reactivation in Poroelastic Rocks*. Dissertation (tu delft), Delft University of Technology.
Novikov, A., Voskov, D., Khait, M., Hajibeygi, H. and Jansen, J. [2022] A scalable collocated finite volume scheme for simulation of induced fault slip. *Journal of Computational Physics*, **469**.
Pluymakers, A., Muntendam-Bos, A.G. and Niemeijer, A. [2023] Induced seismicity: a global phenomenon with special relevance to the Dutch subsurface. *Netherlands Journal of Geosciences*, **102**.
Rohmer, J., Pluymakers, A. and Renard, F. [2016] Mechano-chemical interactions in sedimentary rocks in the context of CO2 storage: Weak acid, weak effects? *Earth-Science Reviews*, **157**, 86 – 110.
Roy, T., Jonsthovel, T.B., Lemon, C. and Wathen, A.J. [2020] A constrained pressure-temperature residual (CPTR) method for non-isothermal multiphase flow in porous media. *SIAM Journal on Scientific Computing*, **42**(4), B1014 – B1040.
Schneider, M., Gläser, D., Flemisch, B. and Helmig, R. [2018] Comparison of finite-volume schemes for diffusion problems. *Oil and Gas Science and Technology*, **73**(1).
Schultz, R., Muntendam-Bos, A., Zhou, W., Beroza, G.C. and Ellsworth, W.L. [2022] Induced seismicity red-light thresholds for enhanced geothermal prospects in the Netherlands. *Geothermics*, **106**, 102580.
Segall, P., Grasso, J.R. and Mossop, A. [1994] Poroelastic stressing and induced seismicity near the Lacq gas field, southwestern France. *Journal of Geophysical Research*, **99**(B8), 15,423–15,438.
Settari, A. and Mourits, F. [1998] A Coupled Reservoir and Geomechanical Simulation System. *SPE Journal*, **3**(3), 219–226.
Shapiro, S., Krüger, O., Dinske, C. and Langenbruch, C. [2011] Magnitudes of induced earthquakes and geometric scales of fluid-stimulated rock volumes. *Geophysics*, **76**(6), WC55–WC63.
Shokrollahzadeh Behbahani, S., Hajibeygi, H., Voskov, D. and Jansen, J. [2022] Smoothed embedded finite-volume method (sEFVM) for modeling contact mechanics in deformable faulted and fractured porous media. *Journal of Computational Physics*.
Sokolova, I., Bastisya, M. and Hajibeygi, H. [2019] Multiscale finite volume method for finite-volume-based simulation of poroelasticity. *Journal of Computational Physics*, **379**, 309–324.
Stefansson, I., Berre, I. and Keilegavlen, E. [2020] Finite volume discretisation of fracture deformation in thermo-poroelastic media. **323**, 519 – 526.
Stefansson, I., Berre, I. and Keilegavlen, E. [2021] A fully coupled numerical model of thermo-hydro-mechanical processes and fracture contact mechanics in porous media. *Computer Methods in Applied Mechanics and Engineering*, **386**, 114122.

Terekhov, K. [2020] Cell-centered finite-volume method for heterogeneous anisotropic poromechanics problem. *Journal of Computational and Applied Mathematics*, **365**.

Terekhov, K., Mallison, B. and Tchelepi, H. [2017] Cell-centered nonlinear finite-volume methods for the heterogeneous anisotropic diffusion problem. *Journal of Computational Physics*, **330**, 245–267.

Terekhov, K. and Tchelepi, H. [2020] Cell-centered finite-volume method for elastic deformation of heterogeneous media with full-tensor properties. *Journal of Computational and Applied Mathematics*, **364**.

Terekhov, K.M. and Vassilevski, Y.V. [2022] Finite volume method for coupled subsurface flow problems, II: Poroelasticity. *Journal of Computational Physics*, **462**.

Tripuraneni, S., Novikov, A. and Voskov, D. [2023] Nonlinear finite volume discretization of geomechanical problem. *International Journal for Numerical and Analytical Methods in Geomechanics*, **47**(12), 2283 – 2303.

Verruijt, A. [2016] *Theory and problems of poroelasticity*. Delft University Press.

Voskov, D., Saifullin, I., Wapperom, M., Tian, X., Palha, A., Orozco, L. and Novikov, A. [2023] open Delft Advanced Research Terra Simulator (open-DARTS).

Wallis, J., Kendall, R. and Little, T. [1985] Constrained residual acceleration of conjugate residual methods. 415 – 428.

Wang, Y., Voskov, D., Khait, M. and Bruhn, D. [2020] An efficient numerical simulator for geothermal simulation: A benchmark study. *Applied Energy*, **264**.

White, J., Castelletto, N. and Tchelepi, H. [2016] Block-partitioned solvers for coupled poromechanics: A unified framework. *Computer Methods in Applied Mechanics and Engineering*, **303**, 55–74.

White, J.A., Castelletto, N., Klevtsov, S., Bui, Q.M., Osei-Kuffuor, D. and Tchelepi, H.A. [2019] A two-stage preconditioner for multiphase poromechanics in reservoir simulation. *Computer Methods in Applied Mechanics and Engineering*, **357**.

Zhao, Y. and Borja, R. [2020] A continuum framework for coupled solid deformation–fluid flow through anisotropic elastoplastic porous media. *Computer Methods in Applied Mechanics and Engineering*, **369**.

Zoback, M. [2007] *Reservoir Geomechanics*. Cambridge University Press.